

# Efficient Oxygen Electrocatalyst for Zn–Air Batteries: Carbon Dots and $\text{Co}_9\text{S}_8$ Nanoparticles in a N,S-Codoped Carbon Matrix

Peng Zhang,<sup>†</sup> Duan Bin,<sup>†</sup> Ji-Shi Wei,<sup>†</sup> Xiao-Qing Niu,<sup>†</sup> Xiao-Bo Chen,<sup>‡</sup> Yong-Yao Xia,<sup>†</sup> and Huan-Ming Xiong<sup>\*,†</sup>

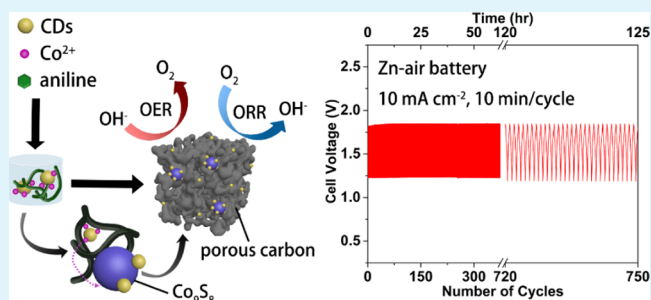
<sup>†</sup>Department of Chemistry and Shanghai Key Laboratory of Molecular Catalysis and Innovative Materials, Fudan University, Shanghai 200433, P. R. China

<sup>‡</sup>School of Engineering, RMIT University, Carlton 3053, Victoria, Australia

## Supporting Information

**ABSTRACT:** Non-noble metal-based bifunctional electrocatalysts for both oxygen reduction reactions (ORRs) and oxygen evolution reactions (OERs) are an essential component of high-performance rechargeable Zn–air batteries (ZABs). Herein, we report a novel and simple method for preparing  $\text{Co}_9\text{S}_8$  nanoparticles embedded in N and S codoped carbon materials with aid of carbon dots (CDs). CDs play a key role in distributing  $\text{Co}_9\text{S}_8$  nanoparticles in the matrix uniformly and enhancing the specific surface area and the electric conductivity simultaneously. The obtained  $\text{Co}_9\text{S}_8/\text{CD}@\text{NSC}$  exhibits an excellent ORR and OER bifunctional catalytic activity and a great long-term durability, with a half-wave potential of 0.84 V versus reversible hydrogen electrode (RHE) for the ORR and a low potential of 1.62 V versus RHE at  $10 \text{ mA cm}^{-2}$ , which outperform the popular Pt/C and  $\text{RuO}_2$  commercial catalysts. Moreover, the  $\text{Co}_9\text{S}_8/\text{CD}@\text{NSC}$  catalyst also displays a superior activity and cycling stability as a cathode material in ZABs, which is far better than Pt/C +  $\text{RuO}_2$  mixture catalysts. Such a ZAB shows a low charge/discharge voltage gap of 0.62 V and great cycling stability over 125 h at  $10 \text{ mA cm}^{-2}$ .

**KEYWORDS:** carbon dots,  $\text{Co}_9\text{S}_8$  nanoparticles, oxygen evolution, oxygen reduction, zinc–air batteries



## 1. INTRODUCTION

The booming demands of electric vehicles and portable electronic devices require upgradation of current energy storage systems, among which rechargeable metal–air batteries have received worldwide attention because of their high energy density and environmental benignancy.<sup>1,2</sup> Particularly, Zn–air batteries (ZABs) are considered as a more practical solution to sustainable energy supply given the low production cost, high safety, and environmental friendliness derived from the use of Zn metal anodes and aqueous electrolyte solution in comparison to Li- or Na-based batteries.<sup>3</sup> However, the expected service performance of ZABs is significantly hindered by the sluggish kinetics of the oxygen reduction reaction (ORR) and oxygen evolution reaction (OER) on the cathode during charge/discharge processes.<sup>4</sup> Therefore, bifunctional oxygen reaction electrocatalysts are desired to overcome the activation energy and accelerate the reactions during the charging/discharging cycles.<sup>5</sup> Currently, precious metal-based electrocatalysts, for instance platinum (Pt) and ruthenium (Ru) or iridium (Ir) oxides, are developed as electrocatalysts for the ORR and OER, respectively.<sup>6,7</sup> However, their high activity is related to either the ORR or OER.<sup>8</sup> In addition, the high production cost and poor durability always hinder their wide applications.<sup>9,10</sup> Therefore, it is vital to develop low-cost,

highly efficient, and durably bifunctional ORR and OER electrocatalysts.

In the past decade, there have emerged various non-noble metal catalysts including transition-metal oxides/chalcogenides/pnictides,<sup>11–13</sup> organometallics,<sup>14,15</sup> and carbonaceous materials.<sup>16–19</sup> Of these materials, transition-metal sulfides (TMSs) have attracted great attention because of their excellent catalytic activity and relatively low cost.<sup>20,21</sup> It was found that cobalt sulfides possess the highest activity for oxygen reactions of all TMSs, especially  $\text{Co}_9\text{S}_8$  which was predicted by theoretic calculations to possess good kinetics like Pt/C for the ORR in acidic solutions.<sup>22</sup> Unfortunately, the  $\text{Co}_9\text{S}_8$ -based catalysts are suffering from a weak catalytic activity and poor durability in long-term service, owing to their low electric conductivity, small surface area, and heavy aggregation.<sup>23</sup> To overcome these drawbacks, scientists have proposed a number of strategies to develop highly active  $\text{Co}_9\text{S}_8$ -based electrocatalysts. Loading  $\text{Co}_9\text{S}_8$  on a conductive carbon support or embedded in a nanoporous substrate such as  $\text{TiO}_2$  is a sound strategy to avoid aggregation of  $\text{Co}_9\text{S}_8$

**Received:** December 26, 2018

**Accepted:** March 26, 2019

**Published:** April 3, 2019

nanoparticles and improve the overall conductivity.<sup>24–26</sup> For example, Dai et al. synthesized  $\text{Co}_{1-x}\text{S}$  nanoparticles on reduced graphene oxide, and the obtained hybrid showed a higher ORR activity than neat  $\text{Co}_{1-x}\text{S}$ .<sup>24</sup> However, bonding between cobalt sulfide and the carbon support is normally too weak to generate efficient electron transfer at interface, and the low surface area leads to insufficient exposure of active centers. Later, Wang et al. treated  $\text{Co}_9\text{S}_8$ –graphene hybrid with  $\text{NH}_3$  plasma to create more active sites and increase their surface area.<sup>27</sup> In addition, Zhang et al. used a Co-containing MOF precursor to obtain  $\text{Co}_9\text{S}_8$  nanoparticles adhered on the carbon matrix.<sup>28</sup> Such in situ growth of  $\text{Co}_9\text{S}_8$  along with carbonization of organic ligands could greatly enhance  $\text{Co}_9\text{S}_8$ –carbon interactions. However, the application of plasma treatments or MOF precursors is not applicable for large-scale production. Some attempts employing cost-effective poly-pyrrole or thiourea as precursors,<sup>29,30</sup> however, prepared  $\text{Co}_9\text{S}_8$  without delicate controls. Therefore, a simple, controllable, and low-cost approach for preparing  $\text{Co}_9\text{S}_8$ -based catalysts remains a challenge.

In the present work, we proposed a simple strategy for growing  $\text{Co}_9\text{S}_8$  nanoparticles with carbon dots (CDs) in the N and S codoped carbon matrix. The product is designated as  $\text{Co}_9\text{S}_8/\text{CD}@\text{NSC}$ . Because CDs can coordinate with  $\text{Co}^{2+}$  ions through their abundant surface functional groups (e.g., hydroxyl and carboxyl),<sup>31,32</sup> the adhesion of CDs on  $\text{Co}_9\text{S}_8$  nanoparticles effectively suppressed their growth and aggregation. Meanwhile, the improved  $\text{Co}_9\text{S}_8$ –carbon interfaces increased both stability and conductivity of the composite system. Moreover, the cross-linking of CDs between PANI fibers realized a high specific surface area.<sup>33,34</sup> Consequently, the  $\text{Co}_9\text{S}_8/\text{CD}@\text{NSC}$  composite catalyst exhibited a superior ORR and OER bifunctional activity with an energy gap ( $\Delta E$ ) of 0.78 V between the ORR half-wave potential (0.84 V vs RHE) and OER potential (1.62 V vs RHE) at a current density of  $10 \text{ mA cm}^{-2}$ , which are close to or exceed the commercial benchmarks (20 wt % Pt/C for the ORR and  $\text{RuO}_2$  for the OER). When  $\text{Co}_9\text{S}_8/\text{CD}@\text{NSC}$  was applied as cathode in a rechargeable ZAB, longer cycle spans and better performances than  $\text{Co}_9\text{S}_8@\text{NSC}$  and the mixture of Pt/C and  $\text{RuO}_2$  were yielded. Such a first attempt of employing CDs for improving both ORR and OER catalysis activities of cobalt sulfides demonstrates a great practical potential for high-performance of ZARs.

## 2. EXPERIMENTAL SECTION

**2.1. Preparation of CDs.** CDs were prepared hydrothermally based on a previously reported method.<sup>35</sup> Typically, 3.07 g of citric acid and 0.96 g of ethylenediamine were dissolved in 30 mL of deionized water and transferred to a 50 mL of stainless-steel autoclave with Teflon-lining, followed by heating at 200 °C for 8 h. After natural cooling of the reaction system to room temperature, the obtained solution was concentrated and then added into excess ethanol and vigorously stirred. After continuous stirring for 5 min, the solution was centrifuged to obtain sediment. After drying, the sediment was dissolved in water and dialyzed against water using a dialysis bag (Spectrum, MW cutoff 3500). Finally, the CDs solution was lyophilized for further use.

**2.2. Preparation of Catalysts.** In a typical procedure of synthesizing  $\text{Co}_9\text{S}_8/\text{CD}@\text{NSC}$ , 0.66 g of aniline was dissolved in 5 mL of 2 M HCl solution, and then 0.16 g of CDs and 0.21 g of  $\text{CoCl}_2 \cdot 6\text{H}_2\text{O}$  were added in the above solution under vigorous stirring to form solution I. Solution II was prepared by dissolving 1.62 g of ammonium persulfate in 5 mL of 2 M HCl solution. Both solutions I and II were placed in an ice-water bath for 10 min to control the

temperature below 5 °C. Subsequently, solution II was quickly added into solution I under vigorous stirring for 1 min and then kept still. After 20 min, aniline was completely polymerized and the mixture turned into a stable PANI hydrogel. The hydrogel was aged for 24 h at room temperature, followed by freeze-drying. The dried aerogel was then transferred into a tube furnace for calcination. The temperature of the furnace was increased from room temperature to 900 °C at a rate of 3 °C/min, and kept at 900 °C for 1 h under nitrogen gas flow. The obtained solid was leached in 0.5 M of  $\text{H}_2\text{SO}_4$  for 8 h, then washed with copious water, and finally vacuum-dried at 80 °C overnight. Finally, the sample was further calcinated at 900 °C for 3 h under a nitrogen flow. In terms of synthesis of  $\text{Co}_9\text{S}_8@\text{NSC}$ ,  $\text{CD}@\text{NSC}$ , and NSC, same procedures were conducted except that there was no CDs or  $\text{CoCl}_2 \cdot 6\text{H}_2\text{O}$  added.

**2.3. Electrochemical Experiments.** All electrochemical measurements were conducted in a three-electrode cell at room temperature using an electrochemical workstation (CH Instruments 660E, Chenhua Co.). The working electrode was prepared by coating catalyst inks on a rotating disk electrode (RDE, Pine Research Instrumentation, USA) with a diameter of 5.0 mm. The catalyst ink was prepared by dispersing 5 mg of catalysts powder and 25  $\mu\text{L}$  of 5% Nafion solution (DuPont) in 1.0 mL of ethanol, followed by ultrasonication for 30 min. Then, 10  $\mu\text{L}$  of the obtained catalyst ink was added dropwise onto RDE and dried naturally. For commercial Pt/C catalyst, the ink was prepared by dispersing 2 mg of catalyst and 10  $\mu\text{L}$  of Nafion (5%) into 1 mL of water/ethanol (1:1) through sonication for 30 min. Then, same procedures were conducted as that of as-prepared catalyst counterparts. A mercury/mercury oxide (Hg/HgO) electrode was used as the reference electrode, and a Pt plate was used as the counter electrode. For consistency, all referred potentials were converted to the reversible hydrogen electrode (RHE) scale using the following formula:  $E$  versus RHE =  $E$  versus Hg/HgO + 0.0591  $\times$  pH + 0.14 V.

All electrochemical tests were performed at room temperature in a KOH solution (0.1 M) saturated with  $\text{O}_2$ . For ORR performance tests, cyclic voltammetry experiments were first conducted for 30 cycles at a potential scanning rate of 50  $\text{mV s}^{-1}$  from 0.2 to 1.2 V versus RHE. As for the linear sweep voltammetry (LSV), a scanning rate of 5  $\text{mV s}^{-1}$  was adopted within the potential range from 0.9 to 0.2 V versus RHE, with rotating rates from 400 to 2025 rounds per minute (rpm). The obtained LSV data were further analyzed using the Koutecky–Levich (K–L) equations

$$\frac{1}{j} = \frac{1}{j_k} + \frac{1}{B\omega^{0.5}} \quad B = 0.62nF(D_{\text{O}_2})^{2/3}\nu^{-1/6}C_{\text{O}_2}$$

in which  $j$  is the measured kinetic current density,  $j_k$  represents the kinetic current density, and  $\omega$  is the rotating rate.  $F$  stands for the Faraday constant ( $96485 \text{ C mol}^{-1}$ ),  $n$  is the electron-transfer number of the ORR,  $D$  ( $1.9 \times 10^{-5} \text{ cm}^2 \text{ s}^{-1}$ ) is the  $\text{O}_2$  diffusion coefficient in 0.1 M of KOH,  $C$  ( $1.2 \times 10^{-6} \text{ mol cm}^{-3}$ ) is the  $\text{O}_2$  concentration when saturated in KOH aqueous solution (0.1 M), and  $\nu$  ( $0.01 \text{ cm}^2 \text{ s}^{-1}$ ) is the electrolyte kinematic viscosity. The K–L plots were derived thereafter at different potentials (0.7 to 0.2 V vs RHE), and then, electron-transfer numbers were calculated from the slopes of K–L plots. For OER performance examinations, LSV tests were conducted at 5  $\text{mV s}^{-1}$  at a rotating rate of 1600 rpm. Tafel plots of the studied catalysts were derived from polarization curves by Tafel equation:  $\eta = a + b \cdot \log j$ , in which  $j$  is the current density,  $b$  is the Tafel slope,  $\eta$  stands for overpotential, and  $a$  represents Tafel constant. The overpotential was calculated using the following equation:  $\eta = E_{\text{RHE}} - 1.23 \text{ V}$ . The stability test was conducted using chronoamperometry at 1.60 V versus RHE with a duration of 40 000 s. Electrochemical impedance spectroscopy (EIS) was conducted with frequencies ranging from  $10^{-2}$  to  $10^5$  Hz with an AC amplitude of 5 mV.

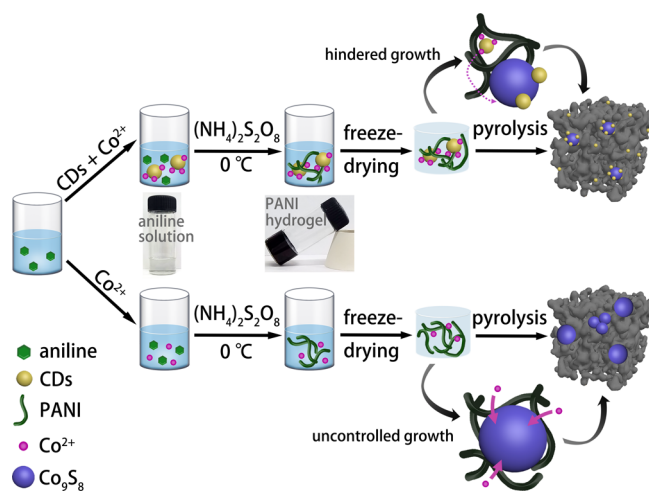
**2.4. Assembling of ZABs.** The rechargeable ZABs were fabricated as follows. First, a mixture of acetylene black and PTFE (mass ratio is 3:2) was pressed on a well-washed Ni foam, which acted as the air diffusion and waterproof layer. Then, the catalysts were loaded on the gas diffusion layer and Ni foam. A Zn foil with a

thickness of 1 mm was used as the anode. The electrolyte used was a mixture of KOH (6 M) and ZnCl<sub>2</sub> (0.2 M) aqueous solution. Then, a two-electrode configuration was assembled, and battery tests were performed under ambient conditions with a Land CT2001 battery testing system.

### 3. RESULTS AND DISCUSSION

The preparation procedures of Co<sub>9</sub>S<sub>8</sub>/CD@NSC and Co<sub>9</sub>S<sub>8</sub>@NSC are shown in Scheme 1. Briefly, polymerization of aniline

**Scheme 1. Schematic Illustration of the Preparation Procedures of Co<sub>9</sub>S<sub>8</sub>/CD@NSC and Co<sub>9</sub>S<sub>8</sub>@NSC**



was initiated by ammonium persulfate with CDs and/or CoCl<sub>2</sub> in HCl solution. PANI hydrogel was formed after several minutes, while the CDs were trapped in networks of PANI hydrogel with adsorbed Co<sup>2+</sup> on the surface. After aging for 24 h, the hydrogel was freeze-dried, followed by calcination, acid-leaching, and a final calcination process. The first calcination carbonized PANI and reduced sulfate ions to form cobalt sulfides. After acid-leaching, the second calcination reinforced the rigidity of the resulting material. For comparison, CD@NSC and NSC compounds were prepared through the same procedures but without CoCl<sub>2</sub> in the precursors.

SEM micrographs (Figure S1) illustrate that all of the materials possess a porous network geometry. Elimination of CDs and cobalt precursors from the reactants leads to the formation of NSC with a spherical microstructure derived from PANI nanofibers. Whilst in the case of CD@NSC, Co<sub>9</sub>S<sub>8</sub>@NSC and Co<sub>9</sub>S<sub>8</sub>/CD@NSC, a higher density of interconnected microstructures is apparent, indicating that CDs or cobalt species facilitate the interactions between PANI nanofibers during the synthesis. Such a cross-linked structure induced by CDs and Co<sub>9</sub>S<sub>8</sub> contributes to the high surface area and pore volumes of the final products. To observe detailed structural features, transmission electron microscopy (TEM) was conducted. It is evident that Co<sub>9</sub>S<sub>8</sub> nanoparticles are wrapped in carbon sheets in both Co<sub>9</sub>S<sub>8</sub>/CD@NSC (Figure 1a) and Co<sub>9</sub>S<sub>8</sub>@NSC (Figure 1b). Obviously, the size of the Co<sub>9</sub>S<sub>8</sub> nanoparticles in Co<sub>9</sub>S<sub>8</sub>/CD@NSC (20–80 nm, with an average size of 38 nm) is greatly smaller than that of Co<sub>9</sub>S<sub>8</sub>@NSC (40–200 nm, with an average size of 105 nm). Such a difference in the microstructure is ascribed to the ion-adsorption effect of CDs,<sup>31</sup> which suppresses the spatial growth of Co<sub>9</sub>S<sub>8</sub> nanoparticles. One solid evidence of adsorption of Co<sup>2+</sup> on CDs is the fluorescence quenching of CDs (Figure

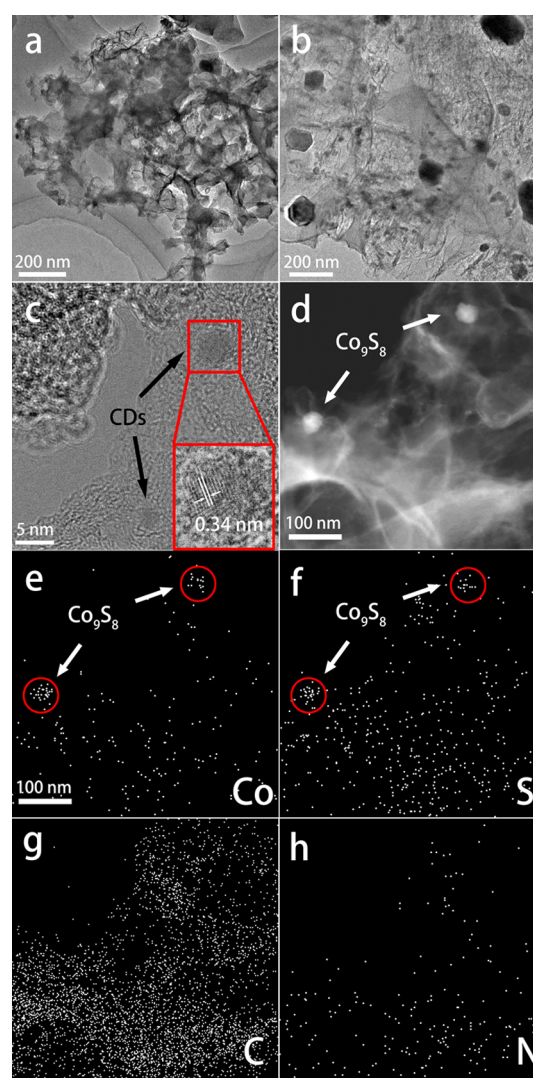


**Figure 1.** TEM images of (a) Co<sub>9</sub>S<sub>8</sub>/CD@NSC and (b) Co<sub>9</sub>S<sub>8</sub>@NSC; (c) HRTEM image of Co<sub>9</sub>S<sub>8</sub>/CD@NSC with a magnified image of CDs (inset); (d) HAADF-STEM images of Co<sub>9</sub>S<sub>8</sub>/CD@NSC, and the corresponding EDX element-mapping images of (e) Co, (f) S, (g) C, and (h) N, respectively.

S3), which can be ascribed to the nonradiative electron transition from CDs to the unoccupied d orbital of Co<sup>2+</sup> ions.<sup>31</sup>

High-resolution TEM (HRTEM) micrographs of Co<sub>9</sub>S<sub>8</sub>/CD@NSC (Figures 1c and 2) demonstrate the coexistence of CDs and Co<sub>9</sub>S<sub>8</sub> nanoparticles with the lattice distance of 0.21

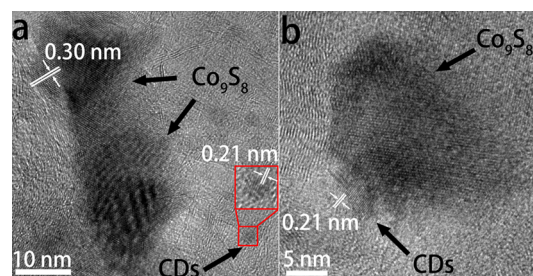


**Figure 2.** (a,b) HRTEM images of Co<sub>9</sub>S<sub>8</sub>/CD@NSC with identification of lattices of both Co<sub>9</sub>S<sub>8</sub> and CDs.

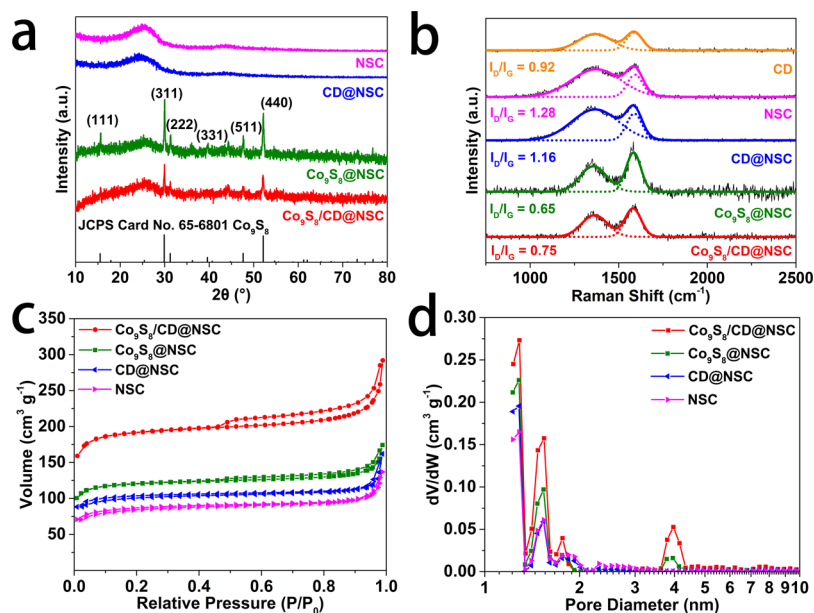


**Figure 3.** (a) XRD patterns and (b) Raman spectra of  $\text{Co}_9\text{S}_8/\text{CD}@NSC$ ,  $\text{Co}_9\text{S}_8@NSC$ ,  $\text{CD}@NSC$ ,  $NSC$ , and  $CDs$ ; (c) nitrogen adsorption–desorption isotherms and (d) PSD calculated by the DFT method of  $\text{Co}_9\text{S}_8/\text{CD}@NSC$ ,  $\text{Co}_9\text{S}_8@NSC$ ,  $\text{CD}@NSC$ , and  $NSC$ , respectively.

nm (assigned to (100) plane of graphite), 0.34 nm (assigned to (002) plane of graphite), and 0.30 nm (assigned to (311) plane of  $\text{Co}_9\text{S}_8$ ), respectively. Furthermore, the distribution of composite elements was studied by high-angle annular dark field scanning TEM (HAADF-STEM), as shown in Figure 1d. Energy-dispersive X-ray (EDX) element-mapping images of  $\text{Co}_9\text{S}_8/\text{CD}@NSC$  (Figure 1e–h) confirm that C and N are homogeneously distributed through the entire structure, in contrast, Co mainly exists at specific areas. As for S, it distributes uniformly in the carbon region and also highly overlaps with Co. Above results indicate the formation of cobalt sulfides and N,S-doped carbon materials.

Crystallographic structures of  $\text{Co}_9\text{S}_8$  and carbon materials were investigated by X-ray diffraction (XRD). As shown in Figure 3a, all of the prepared catalysts present wide diffraction peaks around  $26^\circ$  and  $44^\circ$ , corresponding to the (002) and (101) planes of graphitized carbon materials. Both  $\text{Co}_9\text{S}_8/\text{CD}@NSC$  and  $\text{Co}_9\text{S}_8@NSC$  exhibit characteristic diffraction peaks at  $2\theta$  values of  $15.4^\circ$ ,  $29.8^\circ$ ,  $31.2^\circ$ ,  $39.5^\circ$ ,  $47.6^\circ$ , and  $52.1^\circ$ , corresponding to the (111), (311), (222), (331), (511), and (440) planes of cubic  $\text{Co}_9\text{S}_8$  (JCPDS card no. 65-6801). Those results indicate that the  $\text{Co}_9\text{S}_8$  particles are deposited in a highly graphitic structure. Notably, the peaks of  $\text{Co}_9\text{S}_8$  in  $\text{Co}_9\text{S}_8/\text{CD}@NSC$  have lower intensity and larger FWHM than those in  $\text{Co}_9\text{S}_8@NSC$ , suggesting that  $\text{Co}_9\text{S}_8$  nanoparticles with a smaller size exist in the  $\text{Co}_9\text{S}_8/\text{CD}@NSC$ . According to the Debye–Scherrer formula, the average crystallite size of  $\text{Co}_9\text{S}_8$  nanoparticles in  $\text{Co}_9\text{S}_8/\text{CD}@NSC$  was calculated to be 50.6 nm, while that in  $\text{Co}_9\text{S}_8@NSC$  is 103.4 nm, in accordance with the TEM results. Moreover, the diffraction peaks of graphitic carbon in Co-containing samples are sharper than those of both  $\text{CD}@NSC$  and  $NSC$ , which can be ascribed to the cobalt-catalyzed graphitization of carbon materials.

Raman spectroscopy (Figure 3b) reveals that the intensity ratio of the D band ( $1340\text{ cm}^{-1}$ ) and G band ( $1580\text{ cm}^{-1}$ ) shows an evident decrease from  $NSC$  (1.28) and  $\text{CD}@NSC$  (1.16) to  $\text{Co}_9\text{S}_8@NSC$  (0.65) and  $\text{Co}_9\text{S}_8/\text{CD}@NSC$  (0.75), demonstrating improved graphitization induced by cobalt

species.<sup>36,37</sup> The higher  $I_D/I_G$  value of  $\text{Co}_9\text{S}_8/\text{CD}@NSC$  than  $\text{Co}_9\text{S}_8@NSC$  can be ascribed to the highly defected structure of  $CDs$  ( $I_D/I_G = 0.92$ ). Because the  $I_D/I_G$  value of  $\text{CD}@NSC$  is lower than that of  $NSC$ , it can be speculated that the original structural characteristics of  $CDs$  are retained after preparation. As such,  $CDs$  with a higher graphitization degree promote the  $I_D/I_G$  value of  $\text{CD}@NSC$ . Furthermore,  $CDs$  can also introduce a great number of spatial defects in  $\text{Co}_9\text{S}_8/\text{CD}@NSC$  without deteriorating their highly graphitized backbone structure, leading to a higher  $I_D/I_G$  value than that of  $\text{Co}_9\text{S}_8@NSC$ . As a result, both the highly graphitized substrate and defective sites are favorable for high electron-transfer efficiency and catalytic activity.

Nitrogen adsorption measurements are conducted to investigate the specific surface area and pore structures of the samples. In Figure 3c, the specific surface area of  $\text{Co}_9\text{S}_8/\text{CD}@NSC$  ( $745.2\text{ m}^2/\text{g}$ ) shows a great increment over that of  $\text{Co}_9\text{S}_8@NSC$  ( $468.9\text{ m}^2/\text{g}$ ). Such an increased surface area is ascribed to the cross-linking of  $CDs$  and  $PANI$  fibers. Similarly,  $\text{CD}@NSC$  ( $317.7\text{ m}^2/\text{g}$ ) also shows a larger surface area than  $NSC$  ( $269.3\text{ m}^2/\text{g}$ ). In addition, samples with different quantities of  $CDs$  (namely,  $\text{Co}_9\text{S}_8/\text{CD}0.5@NSC$  and  $\text{Co}_9\text{S}_8/\text{CD}2@NSC$ , with half and twice quantity of  $CDs$  compared with  $\text{Co}_9\text{S}_8/\text{CD}@NSC$ , respectively) were prepared to understand the influence of  $CDs$  on surface area. As shown in Figure S4a and Table S1, the Brunauer–Emmett–Teller specific surface area increases with the addition of  $CDs$ , indicating that  $CDs$  improved the surface area of the prepared materials in an effective manner. Moreover, both cobalt-containing materials exhibit larger surface area than that of pure carbon materials, signifying that the cobalt species are a key contributor to improving surface areas. To unveil more structural characteristics, pore size distribution (PSD) curves are simulated through a density functional theory (DFT) method. As shown in Figure 3d, both  $\text{Co}_9\text{S}_8/\text{CD}@NSC$  and  $\text{Co}_9\text{S}_8@NSC$  possess a hierarchical porous structure with both micropores (1–2 nm) and mesopores (ca. 4 nm), whereas  $\text{CD}@NSC$  and  $NSC$  only exhibit micropores (1–2 nm). The formation of

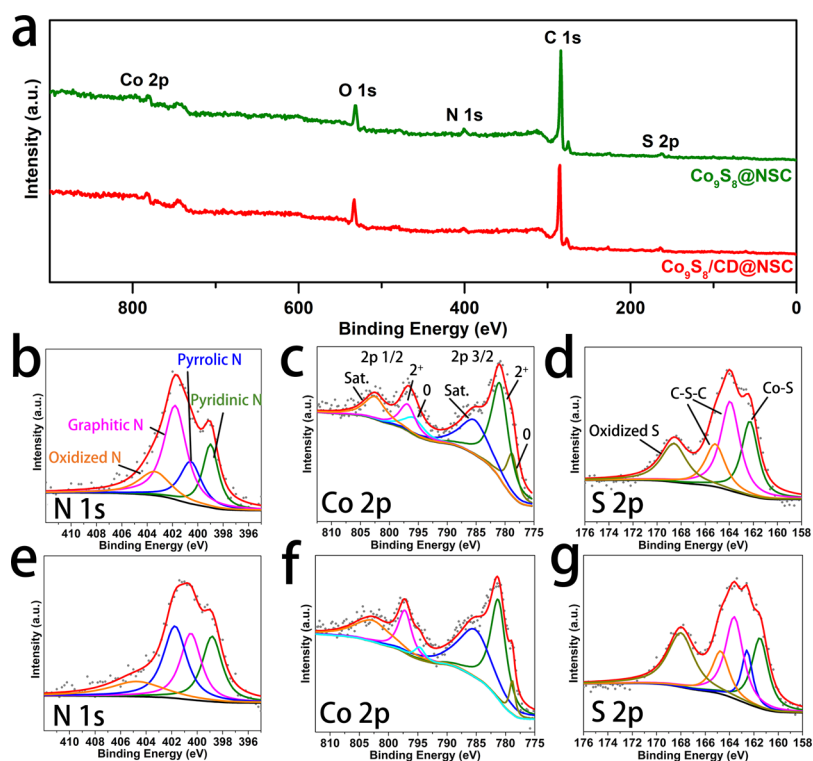


**Figure 4.** (a) XPS broad survey spectra for  $\text{Co}_9\text{S}_8/\text{CD@NSC}$  and  $\text{Co}_9\text{S}_8@\text{NSC}$ , respectively. (b,e) High-resolution XPS spectra of N 1s, (c,f) Co 2p and (d,g) S 2p for  $\text{Co}_9\text{S}_8/\text{CD@NSC}$  and  $\text{Co}_9\text{S}_8@\text{NSC}$ , respectively.

mesopores in Co-containing samples is ascribed to the cobalt-catalyzed activation of carbon.<sup>38</sup> Although both  $\text{Co}^{2+}$  and CDs are beneficial to high surface area,  $\text{Co}_9\text{S}_8/\text{CD@NSC}$  shows a prominently larger increment in surface area than  $\text{Co}_9\text{S}_8@\text{NSC}$  and  $\text{CD@NSC}$ . Such a synergistic effect manifests that the interactions between CDs and  $\text{Co}^{2+}$  are crucial to form a desired porous structure. Furthermore, as shown in Figure S4b and Table S1, the increasing quantity of CDs leads to a larger pore volume and higher average pore size. As such, it is conclusive that CDs facilitate the distribution of  $\text{Co}^{2+}$  in the reaction mixture and further promote the graphitization and structural evolution uniformly, which leads to a highly hierarchical structure.

In addition to structural variations, CDs also endow distinct compositions to the final catalysts. X-ray photoelectron spectroscopy (XPS) full survey spectra (Figures 4a and S5a) show the general elemental compositions of these catalysts. It is evident that all studied materials consist of C, N, and O, whereas S and Co peaks are only observed in  $\text{Co}_9\text{S}_8/\text{CD@NSC}$  and  $\text{Co}_9\text{S}_8@\text{NSC}$ , which confirms that  $\text{Co}_9\text{S}_8$  nanoparticles are incorporated in the N and S codoped carbon matrix. High-resolution XPS spectra of N 1s are plotted in Figures 4b,e and S5b,c, and the results of peak deconvolution are listed in Table 1. Regarding  $\text{Co}_9\text{S}_8/\text{CD@NSC}$ , the N 1s

peak can be deconvoluted into pyridinic N (398.9 eV), pyrrolic N (400.1 eV), graphitic N (401.7 eV), and oxidized N (403.3 eV), respectively.<sup>39</sup> It is well known that both graphitic N and pyridinic N are crucial for ORR and OER activities, whereas pyrrolic N and oxidized N contribute slightly to the catalytic activity.<sup>40,41</sup> As shown in Table 1,  $\text{CD@NSC}$  contains a higher fraction of graphitic N than that of NSC, while their pyridinic N compositions vary slightly. In comparison with NSC,  $\text{Co}_9\text{S}_8@\text{NSC}$  possesses more pyridinic N and a close composition of graphitic N. Those results demonstrate that CDs can introduce more graphitic N to the final catalysts, while cobalt species are favorable for producing pyridinic N. In the case of  $\text{Co}_9\text{S}_8/\text{CD@NSC}$ , fractions of both graphitic N and pyridinic N are higher than those of NSC, that is, the coexistence of CDs and  $\text{Co}_9\text{S}_8$  renders the high concentration of active N species in the catalysts.

Apart from N-doping in the carbon matrix, cobalt sulfide nanoparticles are also key attributes to activating the kinetics of both the ORR and OER. High-resolution XPS spectra of Co 2p (Figure 4c,f) display that two sets of peaks are observed, corresponding to  $2p_{3/2}$  and  $2p_{1/2}$  split peaks, respectively. The peaks at 778.8 and 793.7 eV are ascribed to Co(0), while the peaks at 780.9 and 796.8 eV are characteristics of Co(II).<sup>42,43</sup> Two shake-up satellite peaks centered at 785.2 and 802.5 eV are present, respectively. Such a mixed valence of Co is consistent with the  $\text{Co}_9\text{S}_8$  phase observed in both HRTEM (Figure 2) and XRD (Figure 3a). In addition, high-resolution XPS spectra of S 2p for  $\text{Co}_9\text{S}_8/\text{CD@NSC}$  and  $\text{Co}_9\text{S}_8@\text{NSC}$  (Figure 4d,g, respectively) demonstrate that the peaks at 161.5 and 163.5 eV are ascribed to the Co–S and the C–S–C species, and each of them may split into two peaks corresponding to  $2p_{3/2}$  and  $2p_{1/2}$ , respectively. Furthermore, a peak of oxidized S also appears at ~168 eV.<sup>23,44</sup> These results verify the formation of  $\text{Co}_9\text{S}_8$  in both  $\text{Co}_9\text{S}_8/\text{CD@NSC}$  and

**Table 1.** Peak Assignments and Species Fraction (at. %) for N 1s XPS Spectra

samples	pyridinic	pyrrolic	graphitic	oxidized
$\text{Co}_9\text{S}_8/\text{CD@NSC}$	20.8	18.9	44.3	16.0
$\text{Co}_9\text{S}_8@\text{NSC}$	25.2	26.8	32.3	15.7
$\text{CD@NSC}$	14.1	24.3	49.3	12.3
NSC	13.7	37.6	32.1	16.6

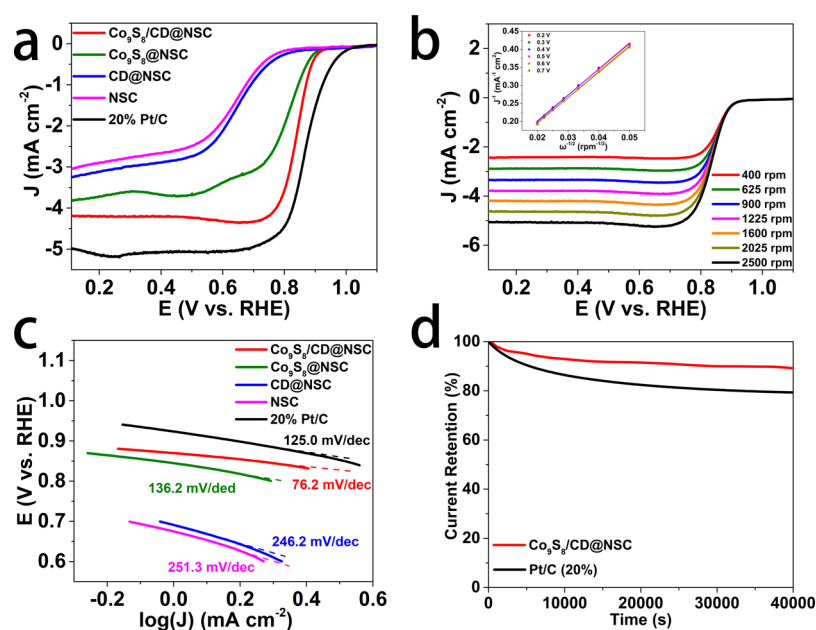


**Figure 5.** (a) ORR polarization of  $\text{Co}_9\text{S}_8/\text{CD@NSC}$ ,  $\text{Co}_9\text{S}_8@\text{NSC}$ ,  $\text{CD@NSC}$ ,  $\text{NSC}$ , and  $\text{Pt/C}$  in an  $\text{O}_2$ -saturated 0.1 M of  $\text{KOH}$  solution with a scan rate of 5 mV/s and a rotation rate of 1600 rpm, respectively; (b) LSV for  $\text{Co}_9\text{S}_8/\text{CD@NSC}$  at different rotation rates varying from 400 to 2500 rpm, and K–L plots derived from LSV results (inset); (c) Tafel plots of all studied catalysts for the ORR (derived from the LSV results); (d) chronoamperometric responses at 0.4 V vs RHE of  $\text{Co}_9\text{S}_8/\text{CD@NSC}$  and  $\text{Pt/C}$ .

$\text{Co}_9\text{S}_8@\text{NSC}$ . In addition, in  $\text{Co}_9\text{S}_8/\text{CD@NSC}$ , CDs, and  $\text{Co}_9\text{S}_8$  are hybridized together in the N, S-codoped carbon matrix, which has a promising potential for ORR–OER bifunctional catalysis.

To evaluate the ORR performances of the catalysts, LSV was performed in  $\text{O}_2$ -saturated 0.1 M of  $\text{KOH}$  solution on a RDE at the rotation rate of 1600 rpm.  $\text{Co}_9\text{S}_8/\text{CD@NSC}$  exhibits a pronounced ORR activity with a more positive half-wave potential (0.84 V vs RHE) than that of  $\text{Co}_9\text{S}_8@\text{NSC}$  (0.79 V vs RHE, Figure 5a). Such an excellent ORR performance is close to the benchmark product, that is, commercial  $\text{Pt/C}$  (0.87 V vs RHE), and is much better than the noncobalt-containing  $\text{CD@NSC}$  and  $\text{NSC}$  catalysts ( $\sim 0.65$  V vs RHE). Even when the preparation of  $\text{NSC}$  was optimized with different annealing temperatures (700–1000 °C), as shown in Figure S6a, their ORR performance only shows slight changes and is still much inferior to the Co-containing samples. By comparing the ORR performances of various catalysts, it is conclusive that  $\text{Co}_9\text{S}_8$  is the main active center in the present work. When CDs are introduced in the catalysts, the ORR performance of both  $\text{CD@NSC}$  and  $\text{Co}_9\text{S}_8/\text{CD@NSC}$  are significantly improved in comparison with their CDs-free counterparts. Such an ORR improvement can be ascribed to the following three aspects. First, the interactions between CDs and PANI fibers during the synthesis render a cross-linked porous structure and a great number of graphitic N species. Second, CDs facilitate uniform distribution of  $\text{Co}^{2+}$  ions in and introduce defective sites to the carbon matrix, realizing a relatively high graphitization degree and a high number density of active centers for catalysis, simultaneously. Finally, CD incorporation enhances the electric conductivity of the entire hybrid compound. To elucidate the roles of each component, we adjusted the content of these species in the hybrid materials and compared their ORR and OER catalytic activities. As shown in Figure S7, the amounts of CDs in  $\text{Co}_9\text{S}_8/\text{CD@NSC}$  were increased as twice as or reduced 50% to obtain  $\text{Co}_9\text{S}_8/$

$\text{CD}2@\text{NSC}$  and  $\text{Co}_9\text{S}_8/\text{CD}0.5@\text{NSC}$ . Meanwhile, the amounts of cobalt precursors were also reduced to 50 or 25% of that in  $\text{Co}_9\text{S}_8/\text{CD@NSC}$  to obtain  $\text{Co}_9\text{S}_8(1/2)/\text{CD@NSC}$  and  $\text{Co}_9\text{S}_8(1/4)/\text{CD@NSC}$ . Then, the ORR polarization curves of these materials were obtained and compared. From Figure S7a it can be seen that increasing the amounts of CDs from zero to one equivalent weight causes a consecutive increase in their ORR activity. However, further addition of CDs results in a decrease in both half-wave potential and limit current. It manifests that CDs have a beneficial contribution to the catalytic activity of as-prepared materials when their amounts were optimized and controlled at a proper value. However, for the role of  $\text{Co}_9\text{S}_8$  nanoparticles, as illustrated in Figure S7c, reducing amounts of cobalt species cause a continuous decrease in ORR catalytic activities. Therefore, it can be deduced that  $\text{Co}_9\text{S}_8$  nanoparticles are the dominant species for activating the ORR.

To seek mechanistic insights into the ORR catalytic activity of  $\text{Co}_9\text{S}_8/\text{CD@NSC}$ , LSV measurements at different rotation rates (400–2500 rpm) were recorded (Figure 5b). The inset K–L plots at different potentials (0.2–0.7 V) are derived from LSV data, and average electron-transfer number is calculated to be 3.92, indicating that a four-electron-transfer pathway of the ORR occurs in  $\text{Co}_9\text{S}_8/\text{CD@NSC}$ . Furthermore, the Tafel plots (Figure 5c) illustrate that  $\text{Co}_9\text{S}_8/\text{CD@NSC}$  possesses the lowest Tafel slope value (76.2 mV/dec), even lower than that of  $\text{Pt/C}$  (125.0 mV/dec). These results demonstrate that  $\text{Co}_9\text{S}_8/\text{CD@NSC}$  has the highest ORR catalytic activity of all samples in this study and is comparable to the  $\text{Pt/C}$  catalyst with respect to kinetics. Long-term stability of  $\text{Co}_9\text{S}_8/\text{CD@NSC}$  for the ORR is also investigated and compared with  $\text{Pt/C}$  by chronoamperometry at a potential of 0.4 V versus RHE. As shown in Figure 5d, the current retention of  $\text{Co}_9\text{S}_8/\text{CD@NSC}$  reaches 89.5% after 40 000 s, larger than that of  $\text{Pt/C}$  (79.1%). These results confirm that  $\text{Co}_9\text{S}_8/\text{CD@NSC}$  is a prominent ORR catalyst with a great potential for long-term applications.

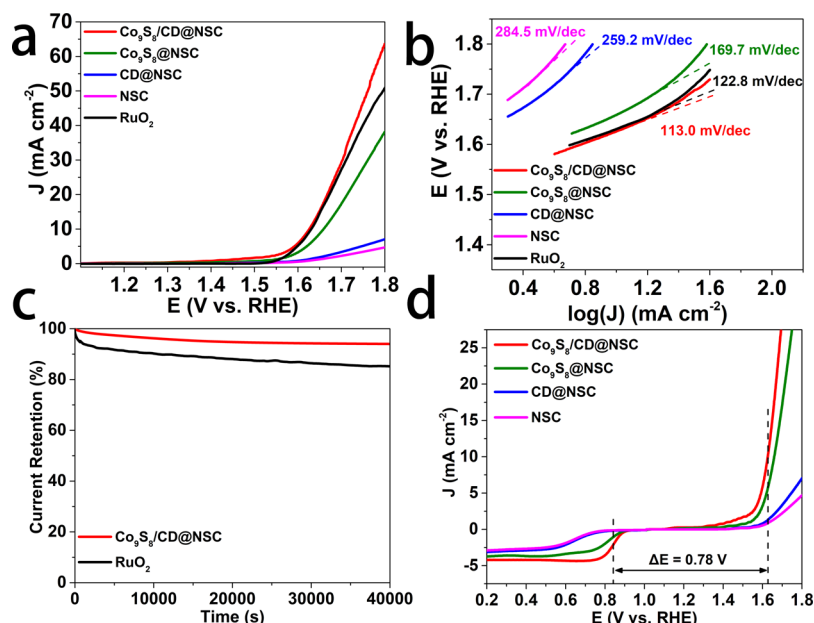


**Figure 6.** (a) OER polarization of  $\text{Co}_9\text{S}_8/\text{CD@NSC}$ ,  $\text{Co}_9\text{S}_8@\text{NSC}$ ,  $\text{CD@NSC}$ ,  $\text{NSC}$ , and  $\text{RuO}_2$  in an  $\text{O}_2$ -saturated  $\text{KOH}$  solution (0.1 M) at a scan rate of 5 mV/s and a rotation rate of 1600 rpm; (b) Tafel plots of all studied catalysts (derived from LSV curves); (c) chronoamperometric responses at 1.6 V vs RHE of  $\text{Co}_9\text{S}_8/\text{CD@NSC}$  and  $\text{RuO}_2$ ; and (d) polarization curves of all studied catalysts in the overall potential range of the ORR and OER ( $\Delta E = E_{1/2} - E_{j=10}$ ).

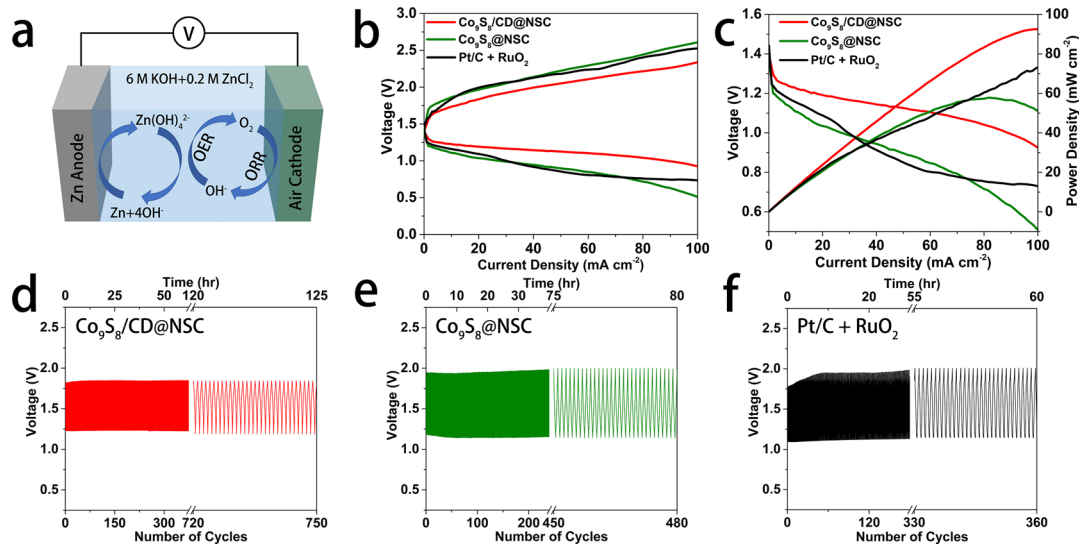


**Figure 7.** (a) Schematic configuration of ZABs; (b) discharge and charge polarization curves of  $\text{Co}_9\text{S}_8/\text{CD@NSC}$ ,  $\text{Co}_9\text{S}_8@\text{NSC}$  and  $\text{Pt/C} + \text{RuO}_2$  mixture, respectively; (c) discharge polarization curves and the corresponding power density plots of the above samples; (d–f) potential profiles against time of the ZABs discharge/charge cycling tests with a current density of  $10 \text{ mA cm}^{-2}$  and a duration time of 10 min for each cycle, employing the above samples as cathode materials.

For OER tests, the polarization potential was extended to 1.8 V versus RHE. As shown in Figures 6a and S6b, LSV measurements were conducted in  $\text{O}_2$ -saturated 0.1 M of  $\text{KOH}$  solution to provide  $\text{O}_2/\text{H}_2\text{O}$  equilibrium at 1.23 V versus RHE. It turns out that the  $\text{Co}_9\text{S}_8$ -free samples show sluggish kinetics for the OER, regardless of the annealing temperature, whereas both  $\text{Co}_9\text{S}_8/\text{CD@NSC}$  and  $\text{Co}_9\text{S}_8@\text{NSC}$  exhibit a promising OER catalytic activity. For comparison, the OER performance of commercial  $\text{RuO}_2$  was evaluated. The potential at the current density of  $10 \text{ mA cm}^{-2}$  ( $E_{j=10}$ ) of  $\text{Co}_9\text{S}_8/\text{CD@NSC}$  is 1.62 V versus RHE, slightly better than that of  $\text{RuO}_2$ , while  $\text{Co}_9\text{S}_8@\text{NSC}$  shows  $E_{j=10}$  of ca. 1.66 V at the same conditions. OER catalytic kinetics were also investigated by the Tafel plots

derived from LSV results. In Figure 6b,  $\text{Co}_9\text{S}_8/\text{CD@NSC}$  possesses the lowest Tafel slope (113.0 mV/dec), much lower than those of  $\text{Co}_9\text{S}_8@\text{NSC}$  (169.7 mV/dec),  $\text{CD@NSC}$  (259.2 mV/dec), and  $\text{NSC}$  (284.5 mV/dec) and even better than that of  $\text{RuO}_2$  (122.8 mV/dec). Similar to the ORR results, reducing the amount of cobalt species can cause a great decrease in the OER activity (Figure S7d). These results prove that  $\text{Co}_9\text{S}_8$  nanoparticles contribute dominantly to the OER activity, while the OER activity of the N and S codoped carbon matrix is negligible. Just like that in the ORR, CDs also show an evident promotion effect in  $\text{Co}_9\text{S}_8/\text{CD@NSC}$  when their amounts were optimized (Figures 6a and S7b), further proving the unique role of CDs in this hybrid material. For the

assessment of their OER catalytic long-term durability, chronoamperometry was conducted at the potential of 1.6 V versus RHE. After 40 000 s, the current density of  $\text{Co}_9\text{S}_8/\text{CD@NSC}$  remains 94.3% of the initial value, whereas the current of  $\text{RuO}_2$  only retains around 84.7%. Subsequently, the electron-transfer resistance of these catalysts was studied through EIS tests.  $\text{Co}_9\text{S}_8/\text{CD@NSC}$  exhibits the smallest semicircular diameter of Nyquist plots, meaning that its charge-transfer resistance is the lowest among all samples (Figure S8). Such a conductivity enhancement is ascribed to the contribution from both CDs and  $\text{Co}^{2+}$ , which improves the graphitization of carbon materials after calcination. In addition to the enhancement in conductivity, the increment in surface area and the reduction of  $\text{Co}_9\text{S}_8$  sizes are also essential for high catalytic activities, and both of them are induced by CDs incorporation.

All of the results prove that  $\text{Co}_9\text{S}_8/\text{CD@NSC}$  is an excellent electrocatalyst for both ORR and OER, better than the state-of-the-art catalysts Pt/C and commercial  $\text{RuO}_2$ . In Figure 6d, the overall polarization curves in the whole oxygen catalysis region are shown to compare the bifunctional performance of all prepared catalysts. The energy gap ( $\Delta E$ ) between the half-wave potential ( $E_{1/2}$ ) of the ORR and the potential at 10  $\text{mA cm}^{-2}$  ( $E_{j=10}$ ) of the OER are deemed as essential standard parameters for bifunctional electrocatalysts.<sup>45–47</sup> Smaller  $\Delta E$  values indicate better reversible performance of catalysts for the oxygen reaction.  $\text{Co}_9\text{S}_8/\text{CD@NSC}$  exhibits the smallest  $\Delta E$  (0.78 V) of all samples of interest, illustrating an excellent bifunctional catalytic activity for the ORR and OER. Moreover, the overpotential of  $\text{Co}_9\text{S}_8/\text{CD@NSC}$  is even smaller than those recently reported bifunctional catalysts based on cobalt sulfides (Table S2).

On the basis of the excellent performance related to both ORR and OER,  $\text{Co}_9\text{S}_8/\text{CD@NSC}$  was used as an air cathode to build a rechargeable ZAB device to measure its performance in a practical service. The ZAB is assembled with a Zn plate anode, Ni foam air cathode coated with catalysts, and electrolyte (6.0 M of KOH aqueous solution containing 0.2 M of  $\text{ZnCl}_2$ ), as shown in Figure 7a. The galvanostatic charge and discharge polarization curves were recorded at varying current densities over a range of 0–100  $\text{mA cm}^{-2}$ . It is evident that the discharge/charge voltage gap of  $\text{Co}_9\text{S}_8/\text{CD@NSC}$  is lower than both Pt/C +  $\text{RuO}_2$  mixture and  $\text{Co}_9\text{S}_8@\text{NSC}$  with the increasing current density (Figure 7b). Moreover, the discharge polarization curves and the corresponding power density curves are plotted in Figure 7c. Apparently,  $\text{Co}_9\text{S}_8/\text{CD@NSC}$  possesses a higher peak power density (92.7  $\text{mW cm}^{-2}$ ) than Pt/C +  $\text{RuO}_2$  mixture (73.2  $\text{mW cm}^{-2}$ ) and  $\text{Co}_9\text{S}_8@\text{NSC}$  (57.9  $\text{mW cm}^{-2}$ ). To assess the long-term discharge/charge cycling performance of the ZAB, continuous galvanostatic discharge/charge tests were carried out at a constant current density of 10  $\text{mA cm}^{-2}$ , and each cycle consisted of 5 min of discharge and 5 min of charge. It reveals that no dramatic changes appear in the discharge/charge voltage of  $\text{Co}_9\text{S}_8/\text{CD@NSC}$  over the entire cycling test period of 125 h, with a voltage gap of 0.62 V at onset and 0.66 V at ending stages (Figure 7d–f), respectively. However, the Pt/C +  $\text{RuO}_2$  mixture displays a growing voltage gap from 0.69 to 0.87 V with running cycles. Moreover,  $\text{Co}_9\text{S}_8@\text{NSC}$  shows a weaker cycling stability and lower activity than  $\text{Co}_9\text{S}_8/\text{CD@NSC}$ , with the charge/discharge voltage gap varying from 0.77 to 0.85 V. Notably, as shown in Figure S9a, there is an evident discharge voltage platform for the ORR in the first six cycles,

while for the charging segment a relatively slow polarization process is observed. At the end of the cycling tests, both charge and discharge voltage platforms are absent. Similar circumstances can also be found in the charge curves of Pt/C +  $\text{RuO}_2$  catalyst at the late stage of cycling tests (Figure S9b).

Considering the compositions of these catalysts, it's speculated that the redox-active species such as Co oxides and  $\text{RuO}_2$  accounts for the disappearance of voltage platforms. The conversion of cobalt sulfides into cobalt oxides during the OER has been well recognized.<sup>48</sup> It has also been reported that a pseudocapacitive nature of highly redox-active catalysts can lead to a higher discharge voltage or a lower charge voltage preceding the regular discharge/charge voltages.<sup>49</sup> Accordingly, it can be deduced that the emerged  $\text{CoO}_x$  or  $\text{CoOOH}$  accounts for the disappearance of voltage platforms. To verify the evolution of  $\text{Co}_9\text{S}_8$  during ZABs charging/discharging, XPS spectra of  $\text{Co}_9\text{S}_8/\text{CD@NSC}$  catalyst after the cycling test were obtained. As shown in Figure S10a, the O elements mainly exist in adsorbed water before the test. While after the ZABs stability tests, in addition to the adsorbed water, there are two new peaks corresponding to hydroxyls and Co–O bonds. Such changes indicate that cobalt oxides/hydroxides emerged after the ZABs stability tests. As for the S element, as shown in Figure S10b,  $\text{SO}_x$  species consisted of the majority of S elements in the catalyst after the ZABs test, indicating an oxidation process during catalysis. Moreover, the XPS peak corresponding to Co(0) disappears after the stability tests, which also proves the oxidation of  $\text{Co}_9\text{S}_8$  into cobalt oxides/hydroxides. As such, it can be concluded that a part of  $\text{Co}_9\text{S}_8$  species were electrochemically converted into cobalt oxides/hydroxides after ZABs stability tests, which is related with their ORR and OER catalytic mechanisms. In spite of this, the cycling test results prove that  $\text{Co}_9\text{S}_8/\text{CD@NSC}$  has a better long-term cycling stability and activity than the competitive counterparts. In comparison with the reported cobalt sulfide-based ZABs,  $\text{Co}_9\text{S}_8/\text{CD@NSC}$  also shows a higher activity as well as stability (as summarized in Table S3). All of the above results demonstrate that  $\text{Co}_9\text{S}_8/\text{CD@NSC}$  is an excellent bifunctional catalyst for ZABs.

#### 4. CONCLUSIONS

We proposed a simple preparation strategy using CDs to improve the structure of  $\text{Co}_9\text{S}_8$ /carbon hybrid materials and increase their ORR and OER bifunctional activities. The introduction of CDs can reduce the growth and aggregation of  $\text{Co}_9\text{S}_8$  nanoparticles during the synthesis, facilitate their distribution in the carbon matrix, and finally enhance the specific surface area and electric conductivity of the products. By embedding CDs and  $\text{Co}_9\text{S}_8$  nanoparticles together in a N and S codoped carbon matrix, the obtained  $\text{Co}_9\text{S}_8/\text{CD@NSC}$  displays an excellent catalytic activity and long-term durability for both ORR and OER, superior to  $\text{Co}_9\text{S}_8@\text{NSC}$ , commercial Pt/C, and popular  $\text{RuO}_2$  catalysts. When being evaluated as air cathode catalysts in ZABs,  $\text{Co}_9\text{S}_8/\text{CD@NSC}$  shows a high activity and long-term cycling stability, better than the performances of the Pt/C and  $\text{RuO}_2$  mixture. Therefore, our work offers a new premise for designing non-noble metal-based ORR and OER bifunctional catalysts applied in ZABs.

#### ■ ASSOCIATED CONTENT

##### Supporting Information

The Supporting Information is available free of charge on the ACS Publications website at DOI: 10.1021/acsami.8b22557.

Additional characterization results of SEM, TEM, XPS, PL spectra, EIS, and comparison results (PDF)

## AUTHOR INFORMATION

### Corresponding Author

\*E-mail: hmxiang@fudan.edu.cn.

### ORCID

Peng Zhang: 0000-0003-1254-3945

Duan Bin: 0000-0002-4142-9052

Xiao-Bo Chen: 0000-0002-4508-5971

Yong-Yao Xia: 0000-0001-6379-9655

Huan-Ming Xiong: 0000-0002-3118-942X

### Notes

The authors declare no competing financial interest.

## ACKNOWLEDGMENTS

This work was supported by the National Natural Science Foundation of China (21771039) and the Shanghai Science and Technology Committee (16DZ2270100).

## REFERENCES

- (1) Bruce, P. G.; Freunberger, S. A.; Hardwick, L. J.; Tarascon, J. M. Li-O<sub>2</sub> and Li-S Batteries with High Energy Storage. *Nat. Mater.* **2011**, *11*, 19–29.
- (2) Steele, B. C. H.; Heinzl, A. Materials for Fuel-Cell Technologies. *Nature* **2001**, *414*, 345–352.
- (3) Lee, J.-S.; Tai Kim, S.; Cao, R.; Choi, N.-S.; Liu, M.; Lee, K. T.; Cho, J. Metal-Air Batteries with High Energy Density: Li-Air Versus Zn-Air. *Adv. Energy Mater.* **2011**, *1*, 34–50.
- (4) Wang, Z.-L.; Xu, D.; Xu, J.-J.; Zhang, X.-B. Oxygen Electrocatalysts in Metal-Air Batteries: From Aqueous to Nonaqueous Electrolytes. *Chem. Soc. Rev.* **2014**, *43*, 7746–7786.
- (5) Zhang, J.; Zhao, Z.; Xia, Z.; Dai, L. A Metal-Free Bifunctional Electrocatalyst for Oxygen Reduction and Oxygen Evolution Reactions. *Nat. Nanotechnol.* **2015**, *10*, 444–452.
- (6) Stamenkovic, V. R.; Fowler, B.; Mun, B. S.; Wang, G.; Ross, P. N.; Lucas, C. A.; Markovic, N. M. Improved Oxygen Reduction Activity on Pt<sub>3</sub>Ni(111) Via Increased Surface Site Availability. *Science* **2007**, *315*, 493–497.
- (7) Lee, Y.; Suntivich, J.; May, K. J.; Perry, E. E.; Shao-Horn, Y. Synthesis and Activities of Rutile IrO<sub>2</sub> and RuO<sub>2</sub> Nanoparticles for Oxygen Evolution in Acid and Alkaline Solutions. *J. Phys. Chem. Lett.* **2012**, *3*, 399–404.
- (8) Li, Y.; Gong, M.; Liang, Y.; Feng, J.; Kim, J. E.; Wang, H.; Hong, G.; Zhang, B.; Dai, H. Advanced Zinc-Air Batteries Based on High-Performance Hybrid Electrocatalysts. *Nat. Commun.* **2013**, *4*, 1805.
- (9) Cherevko, S.; Geiger, S.; Kasian, O.; Kulyk, N.; Grote, J.-P.; Savan, A.; Shrestha, B. R.; Merzlikin, S.; Breitbach, B.; Ludwig, A.; Mayrhofer, K. J. J. Oxygen and Hydrogen Evolution Reactions on Ru, RuO<sub>2</sub>, Ir, and IrO<sub>2</sub> Thin Film Electrodes in Acidic and Alkaline Electrolytes: A Comparative Study on Activity and Stability. *Catal. Today* **2016**, *262*, 170–180.
- (10) Kötz, R. Anodic Iridium Oxide Films. *J. Electrochem. Soc.* **1984**, *131*, 72–77.
- (11) Wang, Y.; Zhou, T.; Jiang, K.; Da, P.; Peng, Z.; Tang, J.; Kong, B.; Cai, W.-B.; Yang, Z.; Zheng, G. Reduced Mesoporous Co<sub>3</sub>O<sub>4</sub> Nanowires as Efficient Water Oxidation Electrocatalysts and Supercapacitor Electrodes. *Adv. Energy Mater.* **2014**, *4*, 1400696.
- (12) Yin, H.; Zhang, C.; Liu, F.; Hou, Y. Hybrid of Iron Nitride and Nitrogen-Doped Graphene Aerogel as Synergistic Catalyst for Oxygen Reduction Reaction. *Adv. Funct. Mater.* **2014**, *24*, 2930–2937.
- (13) Feng, Y. J.; He, T.; Alonso-Vante, N. Carbon-Supported CoSe<sub>2</sub> Nanoparticles for Oxygen Reduction Reaction in Acid Medium. *Fuel Cells* **2009**, *10*, 77–83.
- (14) Odrobina, J.; Scholz, J.; Pannwitz, A.; Francàs, L.; Dechert, S.; Llobet, A.; Jooss, C.; Meyer, F. Backbone Immobilization of the Bis(Bipyridyl)Pyrazolate Diruthenium Catalyst for Electrochemical Water Oxidation. *ACS Catal.* **2017**, *7*, 2116–2125.
- (15) Kadish, K. M.; Frémond, L.; Ou, Z.; Shao, J.; Shi, C.; Anson, F. C.; Burdet, F.; Gros, C. P.; Barbe, J.-M.; Guillard, R. Cobalt(III) Corroles as Electrocatalysts for the Reduction of Dioxygen: Reactivity of a Monocorrole, Biscorroles, and Porphyrin-Corrole Dyads. *J. Am. Chem. Soc.* **2005**, *127*, 5625–5631.
- (16) Sun, X.; Zhang, Y.; Song, P.; Pan, J.; Zhuang, L.; Xu, W.; Xing, W. Fluorine-Doped Carbon Blacks: Highly Efficient Metal-Free Electrocatalysts for Oxygen Reduction Reaction. *ACS Catal.* **2013**, *3*, 1726–1729.
- (17) Yang, L.; Jiang, S.; Zhao, Y.; Zhu, L.; Chen, S.; Wang, X.; Wu, Q.; Ma, J.; Ma, Y.; Hu, Z. Boron-Doped Carbon Nanotubes as Metal-Free Electrocatalysts for the Oxygen Reduction Reaction. *Angew. Chem., Int. Ed.* **2011**, *50*, 7132–7135.
- (18) Ding, W.; Li, L.; Xiong, K.; Wang, Y.; Li, W.; Nie, Y.; Chen, S.; Qi, X.; Wei, Z. Shape Fixing Via Salt Recrystallization: A Morphology-Controlled Approach to Convert Nanostructured Polymer to Carbon Nanomaterial as a Highly Active Catalyst for Oxygen Reduction Reaction. *J. Am. Chem. Soc.* **2015**, *137*, 5414–5420.
- (19) Chen, S.; Duan, J.; Jaroniec, M.; Qiao, S.-Z. Nitrogen and Oxygen Dual-Doped Carbon Hydrogel Film as a Substrate-Free Electrode for Highly Efficient Oxygen Evolution Reaction. *Adv. Mater.* **2014**, *26*, 2925–2930.
- (20) Shao, M.; Chang, Q.; Dodelet, J.-P.; Chenitz, R. Recent Advances in Electrocatalysts for Oxygen Reduction Reaction. *Chem. Rev.* **2016**, *116*, 3594–3657.
- (21) Suen, N.-T.; Hung, S.-F.; Quan, Q.; Zhang, N.; Xu, Y.-J.; Chen, H. M. Electrocatalysis for the Oxygen Evolution Reaction: Recent Development and Future Perspectives. *Chem. Soc. Rev.* **2017**, *46*, 337–365.
- (22) Sidik, R. A.; Anderson, A. B. Co<sub>9</sub>S<sub>8</sub> as a Catalyst for Electroreduction of O<sub>2</sub>: Quantum Chemistry Predictions. *J. Phys. Chem. B* **2006**, *110*, 936–941.
- (23) Qian, H.; Tang, J.; Wang, Z.; Kim, J.; Kim, J. H.; Alshehri, S. M.; Yanmaz, E.; Wang, X.; Yamauchi, Y. Synthesis of Cobalt Sulfide/Sulfur Doped Carbon Nanocomposites with Efficient Catalytic Activity in the Oxygen Evolution Reaction. *Chem.—Eur. J.* **2016**, *22*, 18259–18264.
- (24) Wang, H.; Liang, Y.; Li, Y.; Dai, H. Co<sub>(1-x)</sub>S-Graphene Hybrid: A High-Performance Metal Chalcogenide Electrocatalyst for Oxygen Reduction. *Angew. Chem., Int. Ed.* **2011**, *50*, 10969–10972.
- (25) Ganesan, P.; Ramakrishnan, P.; Prabu, M.; Shanmugam, S. Nitrogen and Sulfur Co-Doped Graphene Supported Cobalt Sulfide Nanoparticles as an Efficient Air Cathode for Zinc-Air Battery. *Electrochim. Acta* **2015**, *183*, 63–69.
- (26) Guo, L.; Deng, J.; Wang, G.; Hao, Y.; Bi, K.; Wang, X.; Yang, Y. P-Doped CoS<sub>2</sub> Embedded in TiO<sub>2</sub> Nanoporous Films for Zn-Air Batteries. *Adv. Funct. Mater.* **2018**, *28*, 1804540.
- (27) Dou, S.; Tao, L.; Huo, J.; Wang, S.; Dai, L. Etched and doped Co<sub>9</sub>S<sub>8</sub>/graphene hybrid for oxygen electrocatalysis. *Energy Environ. Sci.* **2016**, *9*, 1320–1326.
- (28) Li, Y.; Zhou, W.; Dong, J.; Luo, Y.; An, P.; Liu, J.; Wu, X.; Xu, G.; Zhang, H.; Zhang, J. Interface engineered in situ anchoring of Co<sub>9</sub>S<sub>8</sub> nanoparticles into a multiple doped carbon matrix: highly efficient zinc-air batteries. *Nanoscale* **2018**, *10*, 2649–2657.
- (29) Cao, X.; Zheng, X.; Tian, J.; Jin, C.; Ke, K.; Yang, R. Cobalt Sulfide Embedded in Porous Nitrogen-Doped Carbon as a Bifunctional Electrocatalyst for Oxygen Reduction and Evolution Reactions. *Electrochim. Acta* **2016**, *191*, 776–783.
- (30) Huang, S.; Meng, Y.; He, S.; Goswami, A.; Wu, Q.; Li, J.; Tong, S.; Asefa, T.; Wu, M. N-, O-, and S-Tridoped Carbon-Encapsulated Co<sub>9</sub>S<sub>8</sub> Nanomaterials: Efficient Bifunctional Electrocatalysts for Overall Water Splitting. *Adv. Funct. Mater.* **2017**, *27*, 1606585.
- (31) Zhu, S.; Meng, Q.; Wang, L.; Zhang, J.; Song, Y.; Jin, H.; Zhang, K.; Sun, H.; Wang, H.; Yang, B. Highly Photoluminescent

Carbon Dots for Multicolor Patterning, Sensors, and Bioimaging. *Angew. Chem., Int. Ed.* **2013**, *52*, 3953–3957.

(32) Ding, H.; Wei, J.-S.; Xiong, H.-M. Nitrogen and Sulfur Co-Doped Carbon Dots with Strong Blue Luminescence. *Nanoscale* **2014**, *6*, 13817–13823.

(33) Wang, Q.; Wang, H.; Liu, D.; Du, P.; Liu, P. Synthesis of Flake-Shaped Nitrogen-Doped Carbon Quantum Dot/Polyaniline (N-CQD/PANI) Nanocomposites Via Rapid-Mixing Polymerization and Their Application as Electrode Materials in Supercapacitors. *Synth. Met.* **2017**, *231*, 120–126.

(34) Mao, Y.; Bao, Y.; Yan, L.; Li, G.; Li, F.; Han, D.; Zhang, X.; Niu, L. Ph-Switched Luminescence and Sensing Properties of a Carbon Dot–Polyaniline Composite. *RSC Adv.* **2013**, *3*, 5475–5482.

(35) Zhang, P.; Wei, J.-S.; Chen, X.-B.; Xiong, H.-M. Heteroatom-Doped Carbon Dots Based Catalysts for Oxygen Reduction Reactions. *J. Colloid Interface Sci.* **2019**, *537*, 716–724.

(36) Potoczna-Petru, D. The Interaction of Model Cobalt Catalysts with Carbon. *Carbon* **1991**, *29*, 73–79.

(37) Thambiliyagodage, C. J.; Ulrich, S.; Araujo, P. T.; Bakker, M. G. Catalytic Graphitization in Nanocast Carbon Monoliths by Iron, Cobalt and Nickel Nanoparticles. *Carbon* **2018**, *134*, 452–463.

(38) Oya, A.; Yoshida, S.; Alcaniz-Monge, J.; Linares-Solano, A. Formation of Mesopores in Phenolic Resin-Derived Carbon Fiber by Catalytic Activation Using Cobalt. *Carbon* **1995**, *33*, 1085–1090.

(39) Xing, T.; Zheng, Y.; Li, L. H.; Cowie, B. C. C.; Gunzelmann, D.; Qiao, S. Z.; Huang, S.; Chen, Y. Observation of Active Sites for Oxygen Reduction Reaction on Nitrogen-Doped Multilayer Graphene. *ACS Nano* **2014**, *8*, 6856–6862.

(40) Yang, H. B.; Miao, J.; Hung, S. F.; Chen, J.; Tao, H. B.; Wang, X.; Zhang, L.; Chen, R.; Gao, J.; Chen, H. M.; Dai, L.; Liu, B. Identification of Catalytic Sites for Oxygen Reduction and Oxygen Evolution in N-Doped Graphene Materials: Development of Highly Efficient Metal-Free Bifunctional Electrocatalyst. *Sci. Adv.* **2016**, *2*, No. e1501122.

(41) Lai, L.; Potts, J. R.; Zhan, D.; Wang, L.; Poh, C. K.; Tang, C.; Gong, H.; Shen, Z.; Lin, J.; Ruoff, R. S. Exploration of the Active Center Structure of Nitrogen-Doped Graphene-Based Catalysts for Oxygen Reduction Reaction. *Energy Environ. Sci.* **2012**, *5*, 7936–7942.

(42) Xiao, Z.; Xiao, G.; Shi, M.; Zhu, Y. Homogeneously Dispersed Co<sub>9</sub>S<sub>8</sub> Anchored on Nitrogen and Sulfur Co-Doped Carbon Derived from Soybean as Bifunctional Oxygen Electrocatalysts and Supercapacitors. *ACS Appl. Mater. Interfaces* **2018**, *10*, 16436–16448.

(43) Zhu, A.; Tan, P.; Qiao, L.; Liu, Y.; Ma, Y.; Pan, J. Sulphur and Nitrogen Dual-Doped Mesoporous Carbon Hybrid Coupling with Graphite Coated Cobalt and Cobalt Sulfide Nanoparticles: Rational Synthesis and Advanced Multifunctional Electrochemical Properties. *J. Colloid Interface Sci.* **2018**, *509*, 254–264.

(44) Fu, S.; Zhu, C.; Song, J.; Feng, S.; Du, D.; Engelhard, M. H.; Xiao, D.; Li, D.; Lin, Y. Two-Dimensional N,S-Codoped Carbon/Co<sub>9</sub>S<sub>8</sub> Catalysts Derived from Co(OH)<sub>2</sub> Nanosheets for Oxygen Reduction Reaction. *ACS Appl. Mater. Interfaces* **2017**, *9*, 36755–36761.

(45) Wang, T.; Kou, Z.; Mu, S.; Liu, J.; He, D.; Amiin, I. S.; Meng, W.; Zhou, K.; Luo, Z.; Chaemchuen, S.; Verpoort, F. 2D Dual-Metal Zeolitic-Imidazolate-Framework-(ZIF)-Derived Bifunctional Air Electrodes with Ultrahigh Electrochemical Properties for Rechargeable Zinc-Air Batteries. *Adv. Funct. Mater.* **2018**, *28*, 1705048.

(46) Sun, T.; Wang, J.; Qiu, C.; Ling, X.; Tian, B.; Chen, W.; Su, C. N Codoped and Defect-Rich Nanocarbon Material as a Metal-Free Bifunctional Electrocatalyst for Oxygen Reduction and Evolution Reactions. *Adv. Sci.* **2018**, *5*, 1800036.

(47) Liu, S.; Wang, Z.; Zhou, S.; Yu, F.; Yu, M.; Chiang, C.-Y.; Zhou, W.; Zhao, J.; Qiu, J. Metal-Organic-Framework-Derived Hybrid Carbon Nanocages as a Bifunctional Electrocatalyst for Oxygen Reduction and Evolution. *Adv. Mater.* **2017**, *29*, 1700874.

(48) Fan, K.; Zou, H.; Lu, Y.; Chen, H.; Li, F.; Liu, J.; Sun, L.; Tong, L.; Toney, M. F.; Sui, M.; Yu, J. Direct Observation of Structural Evolution of Metal Chalcogenide in Electrocatalytic Water Oxidation. *ACS Nano* **2018**, *12*, 12369–12379.

(49) Sumboja, A.; Lübke, M.; Wang, Y.; An, T.; Zong, Y.; Liu, Z. All-Solid-State, Foldable, and Rechargeable Zn-Air Batteries Based on Manganese Oxide Grown on Graphene-Coated Carbon Cloth Air Cathode. *Adv. Energy Mater.* **2017**, *7*, 1700927.